Orthotropic k-nearest foams for additive manufacturing

Jonàs Martínez, Haichuan Song, Jérémie Dumas, Sylvain Lefebvre

Orthotropic k-nearest foams for additive manufacturing

JONÀS MARTÍNEZ and HAICHUAN SONG, INRIA
JÉRÉMIE DUMAS, Université de Lorraine, INRIA
SYLVAIN LEFEBVRE, INRIA, Université de Lorraine

Fig. 1. 3D printed objects. **Left:** A comfy chair inspired by the work of designer Lilian van Daal. The orthotropic material is oriented to give a soft response on the seat and the back, while keeping other directions rigid. **Right:** Illustrative example of a gear made lighter by filling it with an orthotropic microstructure oriented against the surface to resist pressure.

Additive manufacturing enables the fabrication of objects embedding *metamaterials*. By creating fine-scale structures, the object's physical properties can be graded (e.g. elasticity, porosity), even though a single base material is used for fabrication. Designing the fine and detailed geometry of a metamaterial while attempting to achieve specific properties is difficult. In addition, the structures are intended to fill comparatively large volumes, which quickly leads to large data structures and intractable simulation costs. Thus, most metamaterials are defined as periodic structures repeated in regular lattices. The periodicity simplifies modeling, simulation, and reduces memory costs – however it limits the possibility to smoothly grade properties along free directions.

In this work, we propose a novel metamaterial with controllable, *freely* orientable, *orthotropic* elastic behavior – orthotropy means that elasticity is controlled independently along three orthogonal axes, which leads to materials that better adapt to uneven, directional load scenarios, and offer a more versatile material design primitive. The fine-scale structures are generated procedurally by a stochastic process, and resemble a foam. The absence of global organization and periodicity allows the free gradation of density, orientation, and stretch, leading to the controllable orthotropic behavior. The procedural nature of the synthesis process allows it to scale to arbitrarily large volumes at low memory costs.

We detail the foam structure synthesis, analyze and discuss its properties through numerical and experimental verifications, and finally demonstrate the use of orthotropic materials for the design of 3D printed objects.

CCS Concepts: • **Computing methodologies → Shape modeling**;

Additional Key Words and Phrases: 3D printing, additive manufacturing, procedural modeling, material design, metamaterials

This work is supported by ERC grant ShapeForge (StG-2012-307877).

0730-0301/2017/7-ART121 $15.00
DOI: 10.1145/3072959.3073638

ACM Reference format:
Jonàs Martínez, Haichuan Song, Jérémie Dumas, and Sylvain Lefebvre. 2017. Orthotropic k-nearest foams for additive manufacturing. *ACM Trans. Graph.* 36, 4, Article 121 (July 2017), 12 pages.
DOI: 10.1145/3072959.3073638

1 INTRODUCTION

Additive manufacturing (AM) enables the fabrication of objects having internal microstructures, with feature sizes in the order of tens of microns. The microstructures modify the large scale behavior of the filled volumes, for instance making them lighter but still rigid enough for their intended purpose. Thus, microstructures can be used to fabricate *metamaterials*, the physical properties of which emerge from the local geometric arrangements.

The design of microstructures raises several challenges that directly relate to computer graphics. Their fine and detailed structures, intended to fill comparatively large volumes, quickly lead to tedious modeling, large data structures, and intractable simulation costs. In addition, a major interest in using microstructures with AM is the ability to *grade* material properties within a volume. This affords for materials that can adapt to local conditions, such as being lighter and porous where a part is subject to lower stress. This significantly complicates the design task, as the internal structures have to be specifically tailored for each object.

In this work we propose to focus on microstructures that behave like *orthotropic* materials; that is, their expected elastic behavior differs along orthogonal axes, which can be freely oriented. Orthotropic materials are found in nature: most woods, as well as bones exhibit this behavior. Orthotropy allows the material to better adapt to uneven load scenarios: they can be oriented such that their most rigid axis aligns against the largest stress vectors [Pedersen 1989].

In general, orthotropic materials offer more subtle trade-offs than isotropic ones. Beyond mechanical engineering, they also allow for greater design flexibility as witnessed for instance by the work

of designer Lilian van Daal[1]. Unfortunately, such metamaterials are much more challenging to synthesize and analyze, and to the best of our knowledge no works have yet focused on automatically synthesizing orientable, *orthotropic* graded materials that can be fabricated.

We propose a novel technique to produce microstructures that result in a controlled, freely-orientable orthotropic elastic behavior (see Figure 1). The structures are efficiently generated by a procedural function, without the need for storing or simulating their entire geometry.

Our main contributions are:

- The definition of an orientable, orthotropic foam well suited for modeling and additive manufacturing.
- An efficient procedural evaluation of the microstructures, which is remarkably simple to implement.
- The analysis of the relationship between procedure parameters and elastic properties.

We demonstrate several applications of orthotropic graded foams on 3D printed objects.

2 RELATED WORK

We start by discussing techniques which optimize for material properties within objects in Section 2.1. The output of these methods can be used as a control field for the parameters of a (meta)material defined by a microstructure. We discuss in Section 2.2 microstructures for material design, and in Section 2.3 methods that consider modeling and computational challenges of infilling 3D shapes with microstructures. Finally, we discuss in Section 2.4 approaches that optimize internal structures within objects with similar objectives of rigidity and weight reduction.

2.1 Optimizing for material properties

The field of topology optimization is dedicated to the optimization of material properties within a domain [Eschenauer and Olhoff 2001; Rozvany 2001]. The methods optimizing for continuously spatially-varying material properties (e.g. density) are of direct interest to us [Allaire 2012; Bendsøe and Kikuchi 1988]. After optimization, the question of how to map the continuous, homogenized properties to an actual material arises. Microstructures are one possible approach to this problem [Bendsøe and Kikuchi 1988; Suzuki and Kikuchi 1991]. It is worth noting that topology optimization via homogenization optimizes for a full elasticity tensor at every point (e.g. *free material optimization* [Bendsøe et al. 1994; Kočvara and Stingl 2007], laminate optimization [Allaire and Francfort 1993]), and thus anisotropy information is available. In practice, it is difficult to physically produce materials with this type of control, and this information is often unexploited. One exception is the work of Pantz and Trabelsi [2008], which maps non-regular lattices onto the homogenized solution of a compliance minimization problem. This however requires a global optimization over the domain. Our goal is to provide a metamaterial capable of producing an orthotropic elastic behavior while being simple to conform to a control field – e.g. without having to solve for a global mapping problem.

In computer graphics there is also a strong interest in fabricating deformable, animated objects, as well as interactive editing of such designs. Bickel et al. [2010] design materials with prescribed deformation from a set of predefined base materials. Chen et al.[2013] propose a framework for the optimization of heterogenous multi-material arrangements achieving specific properties. Skouras et al. [2013] optimize for a bi-material distribution to achieve a desired deformation under imposed displacements. Xu et al. [2015] optimize for distributions of different isotropic materials to meet displacement and internal force constraints. Ion et al. [2016] provide an advanced interface to allow users to paint material properties and create mechanisms embedding microstructures.

2.2 Microstructures for (meta)material design

The main approach to make microstructure design tractable is to rely on periodic structures [Sigmund 1994, 1995; Sigmund and Torquato 1999]. This offers two significant advantages. First, the periodicity allows storing in memory a single tile, that is implicitly repeated in a regular grid covering the object. This enables compact storage, efficient display and processing by the AM device (see Section 2.3). Second, the theory of homogenization affords for the computation of the parameters of an *equivalent* homogeneous material [Allaire 2012]. Given these, the object can be simulated while abstracting away fine scale heterogeneities.

The base tile of a periodic microstructure can be optimized through an inverse homogenization problem to target a specific material [Andreassen et al. 2014; Radman et al. 2013; Sigmund 1994; Xia and Breitkopf 2015; Zhou and Li 2008]. Schumacher et al. [2015] extended this methodology to optimize families of periodic tiles with varying properties. Panetta et al. [2015] proposed a family of isotropic tiles based on periodic truss structures. In both these works, tiles with different properties can be spatially arranged to grade properties, such as obtaining varying degrees of elasticity. This requires a special treatment of the boundaries, either ensuring the tile borders are compatible across the entire tile set [Panetta et al. 2015], or performing a global optimization step to choose tiles with best matching borders [Schumacher et al. 2015]. Whenever using a periodic grid care must be taken where the grid intersects the object surface, as tiles are cut by the surface [Robbins et al. 2016].

While extremely efficient and widely adopted, periodic microstructures have a number of disadvantages. The underlying regular grid makes it difficult to smoothly grade the structure properties along arbitrary fields. In particular, when the material is orthotropic, the grid makes it difficult to follow an orientation field seamlessly across grid cells.

Martínez et al. [2016] deviate from periodic microstructures and propose to generate aperiodic, stochastic open-cell foams with prescribed isotropic elasticity, through a procedure akin to solid procedural textures. This builds upon well known properties of open-cell foams [Gibson and Ashby 1997; Roberts and Garboczi 2002], the Young's modulus of which is strongly correlated to their volume (e.g. denser foams produce stiffer materials following a quasi-linear relationship). We discuss in Figure 3 possible ways to obtain an

[1] Chair by designer Lilian van Daal: url.
The chair was manually modeled in Rhinoceros, which took hundreds of hours, see here and here.

orthotropic behavior from such foams, however none proved efficient. Another possibility, not in the Figure, is to rely on *anisotropic* Voronoi diagrams (e.g. [Lévy and Bonneel 2013]). For instance, *Nervous System* uses such diagrams on surfaces to model 3D printed jewelry[1]. However, extraction of curved cell boundaries (edges in 3D) of anisotropic diagrams remains computationally expensive. Disconnected islands may also appear under varying metrics. In comparison, our approach is simple to implement, procedural, and produces structures made of straight beams that exhibit a controlled orthotropic behavior.

2.3 Efficient infilling with microstructures

Given a specific microstructure geometry the question of how to fill a target shape with this detailed geometry arises. Wang et al. [2005] conform truss latices in a thick shell below an object's surface through an efficient procedure that directly outputs a STL model. Rosen [2007] considers the challenges of designing parts with internal lattices and proposes a slicing procedure which works directly from the truss skeleton. Chen [2007] extends texture mapping and signal specialized parameterization to infill volumes with density-varying truss latices. Brennan-Craddock [2011] studies several approaches to apply microstructures within objects, and proposes a slicing algorithm exploiting the periodicity of the structures for efficiency. Pasko et al. [2011] and Fryazinov et al. [2013] explore procedural formulations of periodic microstructures. This enables efficient visualization through ray-tracing, and efficient fabrication by streaming slice images to the printer. Li et al. [2015] rely on such microstructures to optimize the internal cross-sections of an object. Vidimče et al. [2016; 2013] explore a voxel approach to define complex procedural structures within objects, with an emphasis on multi-materials, usability, and slicing efficiency.

Our approach answers the requirements that provide efficient procedural synthesis and direct slicing for scalability of manufacturing. Compared to lattices, we propose a significantly different viewpoint by considering stochastic structures, that do not require solving for a mapping to conform to a vector field. Despite its randomized nature, our approach defines a metamaterial in a principled way, and affords for a precise control of the orthotropic behavior.

2.4 Globally optimized internal structures

A number of approaches optimize internal structures globally. Lu et al. [2014] optimize closed-cell foams formed by the faces of a Voronoi diagram. Wu et al. [2016a] solve for a global, high-resolution topology optimization problem under local material density constraints, which produces porous structures. Wu et al. [2016b] subdivide rhombic structures in a global optimization process, using smaller and denser cells in regions of high compliance. Other approaches optimize sparse truss structures within the volume of objects, such as to obtain rigid but lightweight 3D prints [Wang et al. 2013; Zhang et al. 2015]. Recent software for AM, such as *Autodesk Netfabb*[2], *Autodesk Within*[3] or *nTopology Element*[4], provide the ability to model regular and randomized truss latices that can be globally optimized.

The focus of these global approaches is different from ours: they optimize structures answering a specific scenario, while we seek to define a parameterized *metamaterial*. The metamaterial is only later applied within the object, following a coarse resolution control field, without further optimization – thus metamaterials scale to arbitrarily large volumes.

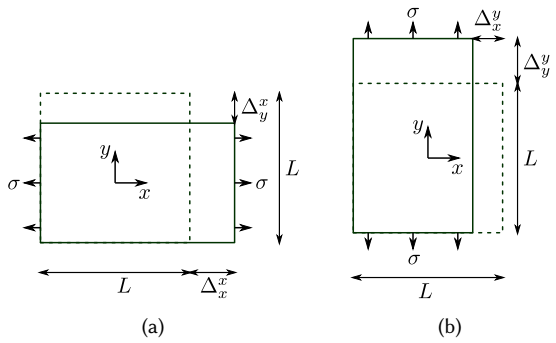

Fig. 2. Uniaxial stress cases for 2D orthotropic materials.
(a) Stress in x direction, $E_x = \frac{\sigma L}{\Delta_x^x}$, $\upsilon_{xy} = -\frac{\Delta_y^x}{\Delta_x^x}$.
(b) Stress in y direction. $E_y = \frac{\sigma L}{\Delta_y^y}$, $\upsilon_{yx} = -\frac{\Delta_x^y}{\Delta_y^y}$.

3 BACKGROUND ON ORTHOTROPIC MATERIALS

This section recalls important notions regarding orthotropic materials. For the sake of clarity we limit the exposition to the 2D case. We provide details for the 3D case in supplemental material. All the formulas consider axis-aligned orthotropic materials. The interested reader can also refer to the text book by Jones [1975] (Chapter 2), and to the work of Li and Barbič [2015] who study orthotropic materials in the context of animation and simulation.

For linear elasticity, the stress-strain relation is $\sigma = C\epsilon$, where C is the elasticity tensor, σ is the stress, and ϵ is the strain. Inversely $\epsilon = S\sigma$, where S is the compliance tensor.

Stress-strain relations. Ideal 2D orthotropic materials are defined by five physical properties: $E_x, E_y, \upsilon_{xy}, \upsilon_{yx}, G_{xy}$, which are respectively the Young's moduli along x/y, the Poisson's ratios (xy/yx), and the shear modulus. Young's moduli and Poisson's ratio are illustrated in Figure 2. We recall below the expression of the compliance tensor S_{ortho}, the expression of C_{ortho} is found by inverting it.

$$S_{ortho} = \begin{pmatrix} s_{11} & s_{12} & 0 \\ s_{12} & s_{22} & 0 \\ 0 & 0 & s_{66} \end{pmatrix} \tag{1}$$

$$s_{11} = \frac{1}{E_x}, \quad s_{22} = \frac{1}{E_y}, \quad s_{12} = -\frac{\upsilon_{xy}}{E_x} = -\frac{\upsilon_{yx}}{E_y}, \quad s_{66} = \frac{1}{G_{xy}}$$

Note that the tensor symmetry ($s_{12} = s_{21}$) leads to:

$$\frac{\upsilon_{xy}}{E_x} = \frac{\upsilon_{yx}}{E_y} \tag{2}$$

Thus, there are only four independent material properties.

[1] http://n-e-r-v-o-u-s.com/blog/?p=7465
[2] https://www.netfabb.com/
[3] http://www.autodesk.com/products/within
[4] http://www.ntopology.com/

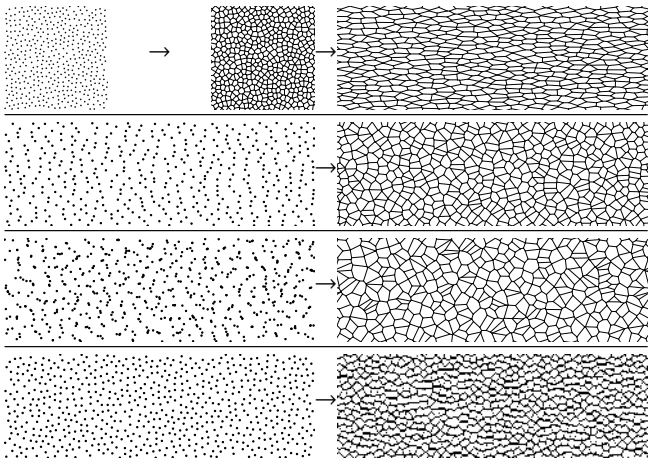

Fig. 3. Inducing orthotropy from isotropic Voronoi foams. Anisotropy is tested numerically. **First row:** A Poisson disc distribution is used to compute a Voronoi diagram that is then stretched (×3). This structure exhibits a good orthotropic elastic behavior, but generalizing the approach would require solving for a global mapping. **Second row:** The Poisson disc distribution is stretched before computing the Voronoi diagram. The structure exhibits little orthotropy. **Third row:** An anisotropic Poisson disc distribution is used to compute a Voronoi diagram. The structure exhibits little orthotropy. **Fourth row:** Voronoi diagram of a Poisson disc distribution, where the beam radii are biased depending on their angle. The final structure exhibits only weak orthotropy (Young's moduli ratio of 1.38 for a radius factor – max over min – of 9.42).

4 PROCEDURAL ORTHOTROPIC FOAM GENERATION

The difficulty to modify Voronoi foams to obtain orthotropy motivated our search for a different type of structure (see Figure 3 and Section 2.2). We retain an open cell-foam design: our structures are made of connected beams. This has advantages regarding fabrication, in particular on powder fusion AM processes (e.g. Selective Laser Sintering, common in industrial applications). The open structure allows non fused material to exit the part.

We generate the foams by first constructing a graph embedded in 2D or 3D (Section 4.1), which is then thickened to obtain the beam structure. The graph does not have to be explicitly constructed and stored. Instead it is generated locally whenever needed, on-the-fly (Section 4.2). The structure is infinite, aperiodic and stochastic. Most importantly, its parameters can be changed locally without globally impacting the structure. This affords for efficient spatial grading and orientation of properties.

For clarity, in the following sections we illustrate the 2D version of our foams. Nevertheless, the description of the procedural generation extends analogously to 3D.

4.1 Graph structure

Our approach for generating orthotropic foams involves two algorithms. The first is a point distribution algorithm, which produces the nodes of the structure. The second algorithm connects the nodes together, producing the skeleton of the beams. Each algorithm has parameters which impact the structure geometry, and ultimately its elastic behavior.

In this work we always use beams of minimal printable thickness. For the same volume this lets us maximize foam density.

Point distribution. Our structures rely on an isotropic point distribution similarly to procedural Voronoi foams [Martínez et al. 2016]. We generate one random point in each cell of a virtual grid covering the space, which provides a crude but efficient approximation of a Poisson disc distribution [Worley 1996]. The subdivision scheme of Martínez et al. [2016] is used to locally increase or decrease the point density.

Edge connections. In absence of anisotropy, we generate the edges of the graph by connecting each point to its k closest neighbors. For sufficiently large values of k (as discussed later), this produces fully connected isotropic structures.

The edges of the graph are the essential component in inducing anisotropy in the elastic behavior of the structures. As seen in Figure 3 (top), a global stretch of an isotropic graph introduces an excellent orthotropy in its elastic response. The effect of the stretch is to bias the angular distribution of edge lengths, making the equivalent material stiffer along the direction with longest edges. Our key insight is to produce a similar bias, and hence a similar elastic response, without having to rely on a global stretch. Instead we introduce local stretches that can be easily controlled. In the limit our approach converges towards an ideal laminate (like a global stretch), which reach orthotropic elasticity bounds [Lipton 1994].

We produce the angular edge length bias by stretching the distance computation when selecting the k-nearest neighbors. This encourages longer edges to appear in the direction of largest stretch, as k-nearest neighbors are selected further away (see the inset below and Figure 4). Section 5 provides an in-depth analysis of the impact of the stretch of metric on the orthotropic elastic behavior.

More precisely, let us consider two points p_i, p_j in the embedded graph in dimension d. We denote the frame orientation at point p as $\Theta(p) : \mathbb{R}^d \rightarrow [0,\pi]^a$, with $a = \{1,3\}$ for respectively the 2D and 3D cases (Euler angles). We denote the stretch at p as $H(p) : \mathbb{R}^d \rightarrow \mathbb{R}^d_+$, which, without loss of generality is assumed to be an ordered length vector. In 2D (h_u, h_v) with $h_u \geqslant h_v$ and $h_v = 1$. In 3D (h_u, h_v, h_w) with $h_u \geqslant h_v \geqslant h_w$ and $h_w = 1$.

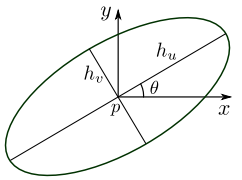

We define the metric tensor as [Du and Wang 2005]:

$$M(p) = E^T U E, \quad E = R(\Theta(p)), \quad U = \mathrm{diag}(H(p)^{-2}) \tag{3}$$

where $R(\Theta)$ is the n dimensional clockwise rotation matrix.

The asymmetric anisotropic distance from p_i to p_j is:

$$d_{p_i}(p_i, p_j) = \sqrt{(p_i - p_j)^T M(p_i)(p_i - p_j)} \tag{4}$$

In order to simplify the synthesis of the structure, we define a symmetric distance $d(p_i, p_j)$ as:

$$d(p_i, p_j) = \frac{d_{p_i}(p_i, p_j) + d_{p_j}(p_j, p_i)}{2} \tag{5}$$

This distance is used to select the k-nearest neighbors, producing an anisotropic distribution of edges. We here conjecture that this translates to an orthotropy in the elasticity tensor. This, however, is

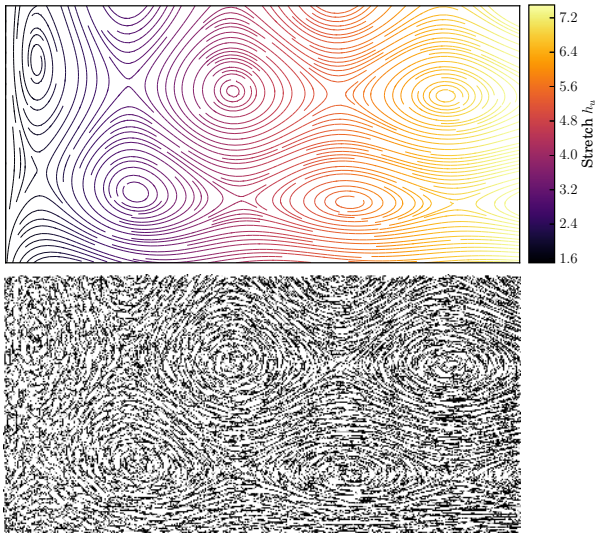

Fig. 4. A varying metric field (top), and the resulting k-nearest microstructure (bottom), $k = 6$.

not obvious. We verify it is the case in Section 5. We also quantify the relationship between the metric anisotropy and the impact on the Young's moduli and Poison's ratios in each direction.

Connectivity. A major concern for fabrication is to obtain fully connected structures. Studies in graph theory indicate that k-nearest random graphs are connected with very high probability for even small values of k [Balister et al. 2005]. Our case is, in fact, more favorable: when using a point distribution similar to Worley [1996] one can easily guarantee that at least one sample exists in each virtual grid cell. In practice we use $k = 6$, which with uniform density always achieves connectivity even with strong anisotropy.

We experimentally evaluate the impact of anisotropy on connectivity by producing random instances of the foam in a finite, large domain. We assume the structure to be attached to the boundary (i.e. the surface of the object), and track for any disconnected component inside. We use a square domain of unit size covered by a grid of 32^2 points, and a maximum tested stretch ratio of $h_u = 80$. The maximum edge length was measured at 0.7. Running 7k tests on stretch ratios from 1 to 80 did not produce any disconnected component.

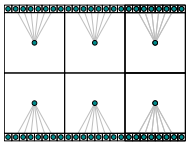

While we did not observe any detrimental effect of anisotropy on connectivity, disconnections may occur when varying density. In fact, following the first steps of the proof in Xue and Kumar [2004], we can easily setup a "trap" as illustrated in the inset. Such a trap consists in sandwiching a narrow band of low density in between two bands of much higher density. As a result, the nodes from the coarse band will take their k-nearest neighbors in the high-density bands only, creating a gap in connectivity. Figure 5 reveals this behavior on our foams. Such cases seldom occur in practice as the density control fields are typically smooth ; if needed the connectivity of the structure can be checked efficiently through a sweeping scheme (line in 2D, slice in 3D) as the structure synthesis is procedural. Larger values of k also alleviate this issue.

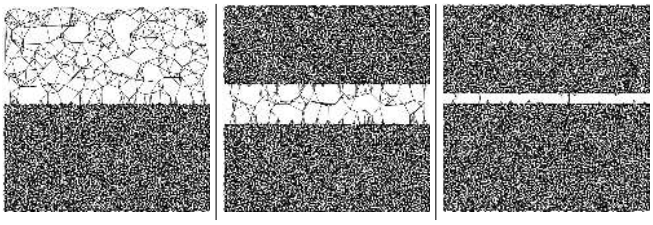

Fig. 5. **Left to right:** Abrupt density change in a k-nearest foam ($k = 6$). The dense part is 64 times denser. As long as the low-density band is not too narrow, the "trap" situation (right most) does not occur.

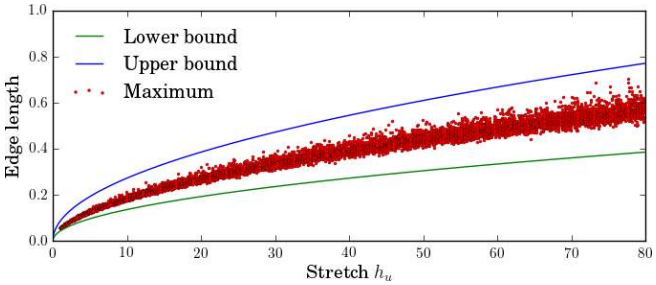

Fig. 6. Edge lengths in a k-nearest foam ($k = 6$), within a jittered grid of size 32×32 covering the unit square. The metric stretch goes up to an (extreme) value of $h_u = 80$. The curves outline the lower and upper bounds.

Locality. Locality is an important property for the efficient evaluation of the foam geometry: we seek for an algorithm where a sub-set of the foam can be generated without having to globally synthesize the result. To achieve this, the search radius (with the usual L_2 distance) to find the k-nearest neighbors of a point has to be bounded.

Since we guarantee one sample per jittered grid cell, such an upper bound exists. Finding a tight upper bound is however difficult. We need to find the smallest radius that will contain at least k points – this relates to the Gauss circle problem generalized for ellipses [Bentkus and Götze 1997; Hardy 1915], but is not strictly the same as we rely on a jittered grid. Nevertheless, from these works we can derive a *lower* bound (the radius that must at least be searched) that is given in 2D by $c \cdot h_u \sqrt{k/(\pi \cdot h_u \cdot h_v)}$, and in 3D by $c \cdot h_u \sqrt[3]{k/(\pi \cdot h_u \cdot h_v \cdot h_w)}$, where c is the grid cell size length. In practice, we observe that the lower bound follows a trend similar to the experimental upper bound, see Figure 6. We therefore set the upper bound proportional to the lower bound, in practice using a factor of 2. As shown Figure 6 the 2D upper bound remains well above the measured edge lengths for the stretch ratios we use. During evaluation we use the bound obtained from the maximum stretch in the control field.

4.2 Procedural evaluation of orthotropic foams

Given the properties of connectivity and locality, we devise a procedural evaluation scheme. A procedural solid texture function, which returns either empty of solid for any coordinate is possible. However

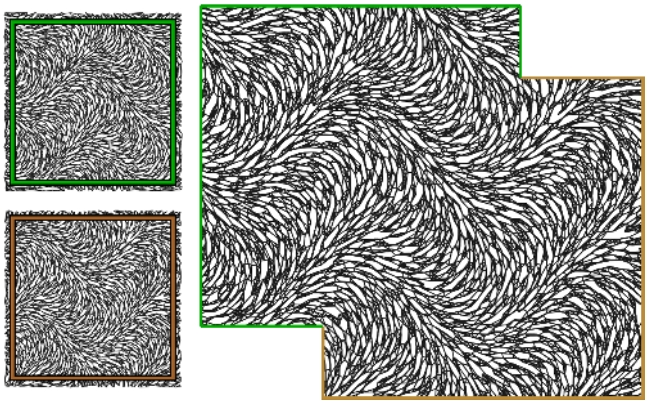

Fig. 7. Foam procedural per-block evaluation. The foam is oriented according to a sine wave pattern. **Left:** Two blocks of foam generated independently for different overlapping regions of space. The foam outside the colored rectangles is ignored after synthesis; it only serves as padding to ensure correct computations inside. **Right:** Overlapping the two blocks produces a seamless result: their content is deterministic and exactly matches in the overlap region. The space spawned by the procedure is infinite.

it would be computationally wasteful due to the repeated k-nearest searches. Instead, we propose a per-block synthesis scheme that groups computations in a local region of space.

Let us assume our point distribution algorithm is pseudo-random and can generate point-sets deterministically in any box in space. This is the case of the jittered grid approach we favor. Let us consider an axis aligned box with min corner c_{min} and max corner c_{max}. To produce the foam geometry within the box $[c_{min}, c_{max}]^d$, we generate the point distribution in an enlarged box $[c_{min}, c_{max}]^d \oplus L_{\max}$ where $\oplus$ is the morphological dilation and $L_{\max}$ is the bound on maximum edge length, computed from the maximal stretch in the field. This guarantees that all the points required for the k-nearest search within the smaller box $[c_{min}, c_{max}]^d$ are available within the enlarged box. Thus, the set of edges matches the set that would have been generated globally. In other words, this evaluation is deterministic: generating the foam in overlapping boxes produces the same geometry within the overlapping regions. This process and its results are shown in Figure 7.

Using this approach, we can efficiently generate the foam in any spatial box, in a time that only depends on the box extent (the foam domain being infinite). In particular, this can be used for front-to-back rendering during visualization, or during slicing for AM where only a thin slab of foam has to be computed [Pasko et al. 2011]. Multiple boxes of foam can be generated in parallel.

5 ANALYSIS OF ORTHOTROPIC FOAMS

For the foams to be useful as a metamaterial it is important that the equivalent material properties correlate to the synthesis parameters. If this relationship exists and can be characterized, one can easily fill a volume with a foam that produces a target elastic behavior.

We use numerical homogenization (Section 5.1) to verify the link between the anisotropy of the foam geometry and the orthotropy of the elasticity tensor (Section 5.2). We then analyze the material space spawned by the foams (Section 5.3) for varying synthesis parameters. We conclude by mechanical tests on printed samples (Section 5.4). We provide additional analysis in supplemental material for homogenization versus detailed simulation and for the isotropic case.

In the remainder, we consider an isotropic base material of Young's modulus $E = 1$ (without loss of generality since the Young's modulus values are linearly proportional to that of the base material). We consider a base Poisson's ratio of $v = 0.3$ which is representative of plastic materials.

5.1 Homogenization

We analyze the macroscale behavior using numerical homogenization in grids of hexahedral (3D) or quad (2D) linear elements. This computes the tensor of an equivalent homogeneous material for a given sample of our foam. We provide additional details on numerical homogenization in the supplemental material.

Similarly to Martínez et al. [2016], we generate periodic versions of the foams in a grid of varying spatial extent, and apply numerical periodic homogenization to each. We fit the homogenized elasticity tensor C_{hom} to an ideal orthotropic tensor C_{ortho} of orientation O (see Section 3), which retrieves both the orthotropic parameters and a fitting error. We increase the spatial extent until the fitting error is negligible, ensuring enough foam is observed to obtain a reliable result (grid of 300^2 elements in 2D, 80^3 in 3D). For now, let us assume the orthotropic orientation O is known. We discuss its selection in Section 5.2.

To perform the fitting we consider the logarithmic Euclidean distance. This has the desirable property of evaluating to the same value for both the elasticity and compliance tensors, and provides more accurate results for elasticity compared to the Frobenius norm [Moakher and Norris 2006]. The logarithmic Euclidean distance for the elasticity tensor is:

$$d_L(C_{ortho}, C_{hom}) = \|\log(C_{ortho}) - \log(C_{hom})\|_F \qquad (6)$$

The optimization is constrained such that C_{ortho} is positive definite [Ting 1996]. We use a gradient-based optimization with nonlinear constraints [Johnson 2016]. Since the objective function involves matrix logarithms, its gradient is computed with numerical differentiation.

5.2 Orientation conjecture

We generate anisotropic foam geometries by locally stretching the metric used to connect a point to its k-nearest neighbors (Section 4.1). In this section we verify that the geometric stretch translates to an orthotropy of same angle in the elasticity tensor. We perform the analysis in 2D.

To observe this, in particular on low stretches, we setup the following numerical experiment. We generate 6800 foam samples for stretch values h_u in $\{1.5, 2.5\}$, where h_u aligns with the horizontal axis, h_v with the vertical axis. We fit an orthotropic tensor to each, rotating the expected angle of orthotropy O (Section 5.1), and considering the fitting error. If the material is indeed orthotropic with direction O, then the fitting error is expected to be small. Otherwise, the fitting error is expected to increase as the directions of orthotropy do not match.

Rather than using absolute values of fitting error, which are difficult to interpret, we consider the normalized measure proposed in [Moakher and Norris 2006]:

$$d_N = \frac{d_L(C_{ortho}, C_{iso})^2}{d_L(C_{hom}, C_{iso})^2} \in [0 \dots 1] \tag{7}$$

where C_{iso} is a fitted isotropic tensor (obtained by the fitting process of Section 5.1, using an idealized isotropic tensor, see supplemental material), and C_{ortho} is the fitted orthotropic tensor. A value of one indicates that the fitted tensor is indeed close to ideally orthotropic, while zero indicates the opposite. A value above 0.9 is considered to be a good agreement [Moakher and Norris 2006].

We perform this analysis for three different uniform point distributions: uniform random coordinates, Poisson disc, and the jittered grid approach we use in practice. Results are reported in Figure 8. As can be seen, for angles where O does not align with the metric stretch the error increases (lower values of d_N), while the agreement is excellent when axes align. This verifies that the stretch in the metric translates to a similarly aligned orthotropy in the material.

Another interesting observation is to consider how randomness impacts the properties (i.e. the spread of points around the average behavior). The spread is wider for a uniform random coordinate distribution, and narrower for Poisson disc, while the jittered grid lies in between. The spread of the jittered grid actually narrows on larger stretch values, and becomes similar to that of the Poisson disc distribution. This indicates that there is little difference in quality between using a jittered grid or a Poisson disc distribution, especially with high orthotropy.

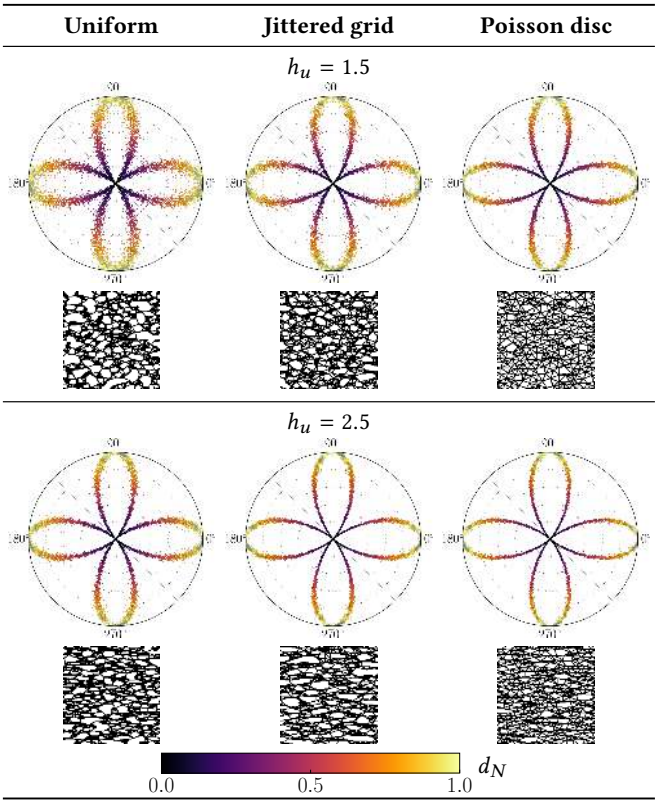

Fig. 8. Numerical verification of the material orthotropy for uniform random coordinates, jittered grid, and Poisson disc point distributions. The normalized measure d_N is plotted against stretch angle O (polar axis in degrees), and used as color code (bottom colorbar).

5.3 Material space

We now analyze the space of materials covered by our technique. We generate a large number of orthotropic 2D samples, and evaluate each with numerical homogenization. We vary the stretch h_u (up to 15 to cover a wide range) and the density. The orientation is fixed to zero since we verified numerically in Section 5.2 the orientation conjecture. We exploit symmetries in orthotropy when exploring the material space. The samples all have the same spatial extent but are randomized: the dataset may contain samples with similar parameters, but they are different random realizations.

The results for the 2D foams are summarized in Figure 9. The variations in normalized Young's moduli along each axis are shown in the top part. An isotropic material would only cover a diagonal, as the orthotropic axes would have the same Young's modulus. Our structures cover the full spectrum of Young's moduli and ratios between them. The main factor in controlling the ratio between the Young's moduli is, as expected, the metric stretch. The main factor in controlling the absolute Young's modulus values is the density.

The plot at the bottom of Figure 9 reveals the behavior of the Poisson's ratio together with the Young's moduli. Figure 9 plots only υ_{xy} as υ_{yx} follows from Equation (2). The Poisson's ratio remains positive, and sharply increases on small volumes and high stretches. Figure 9 contains a foam representative of this case ($\upsilon_{xy} = 5.16$). Since the Poisson's ratio of orthotropic materials is unbounded [Ting and Chen 2005] large values are to be expected.

Figure 10 presents the analysis of Young's moduli on 3D foam samples (cubes). As can be seen, the foams provide a good coverage of possible ratios between E_x, E_y, E_z. We limited the exploration to a stretch of at most 14 in all directions, but the space could be explored further. The Poisson's ratio behaves as with 2D foams. Please refer to the supplemental material for the plots of the 2D and 3D shear modulus, and 3D Poisson's ratio.

In summary, our foams cover the Young's modulus space densely. However, for a fixed orientation of orthotropy, our foams have only two (2D) or three (3D) independently controlled elasticity parameters, so they do not offer a complete control. For instance, in 2D, choosing both Young's moduli fixes the Poisson's ratio and shear modulus. Varying k changes the stiffness for a same density, but does not significantly change the covered material space.

The user selects a foam by specifying a desired pair (2D) or triplet (3D) of Young's modulus. The foam parameters are obtained by interpolating from the three closest samples in our dense datasets (distance weighted interpolation). If any of the three is further than a threshold derived from sampling density, the point is rejected as not covered by the foam pre-computed material space. Projecting to a closest match is left for future work. In 2D, for 13000 randomly tests we obtain an average relative Young's modulus error of 0.84%, and in 3D for 350 tests an error of 2.06%. The higher error in 3D is

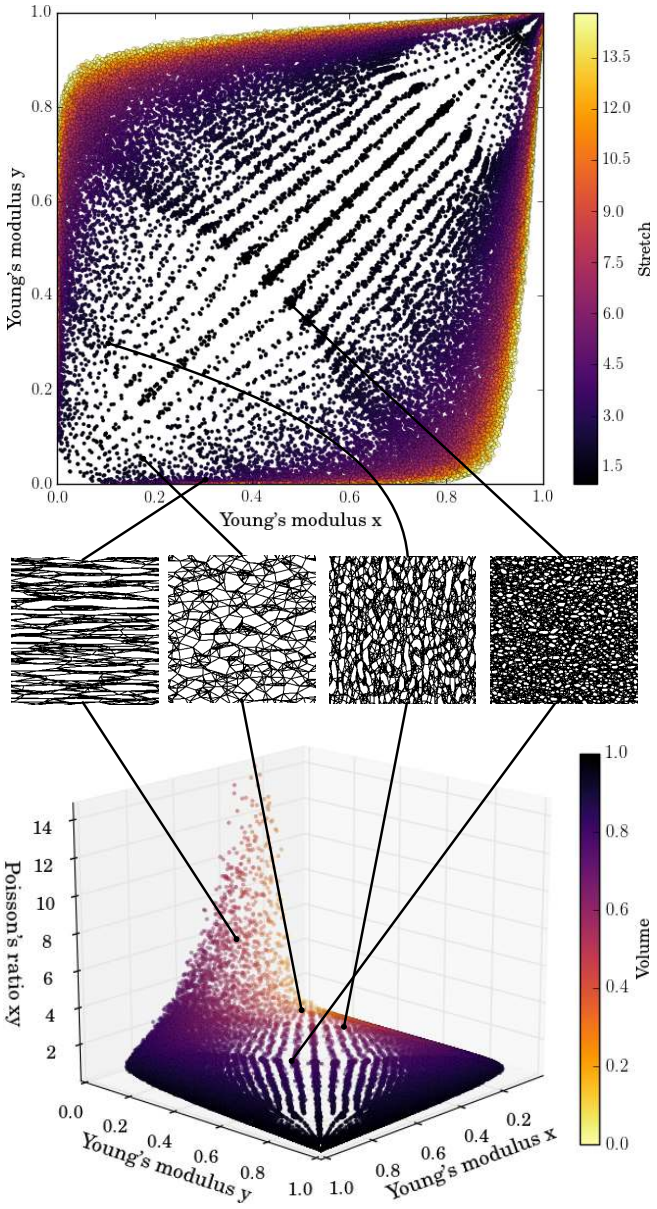

Fig. 9. Material space, please refer to the text for discussion. **Top:** Young's moduli along the main axes of orthotropy, color coded by the metric stretch parameter. The uneven spacing is due to the non-linearity between the sampled parameters and the elastic behavior. **Middle:** Foam samples. **Bottom:** Poisson's ratio xy and Young's moduli.

explained by the lower sampling of the material space.

5.4 Measurements on printed samples

We verify our numerical analysis on actual 3D printed samples. We focus this analysis on 2D versions of the foam, which are vertically extruded to obtain a 3D solid object. We print the structures using *SemiFlex* filament on an *Ultimaker 2+* with a 0.25 mm nozzle, with a custom slicer. Each beam is exactly one filament wide. Please refer

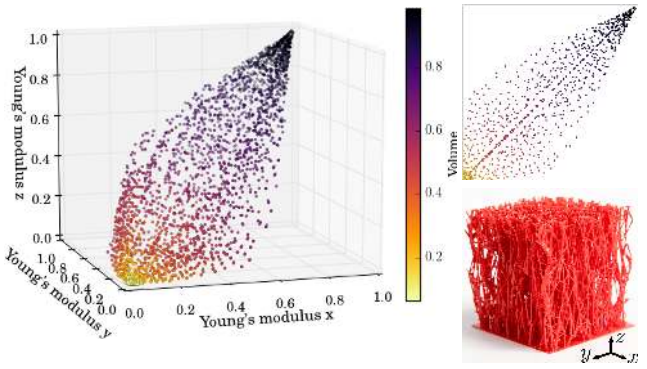

Fig. 10. Covered material space for 3D foams. **Left:** Young's moduli along the three orthogonal axes, color coded by volume. **Top right:** Projection of the Young's moduli along the x and y axes. **Bottom right:** printed sample.

to the supplemental material for details.

We printed a family of samples with varying degrees of metric stretches. We additionally print a full sample, which acts as a reference for the (3D printed) full base material (cross-hatched, 100% infill). The test specifications and results are summarized in Figure 11. Figure 11a shows the raw data measured from the sensor. For fitting the linear material parameters we only use the first half millimeter of displacement (from 0 to 0.5 mm), as the material enters non-linear elasticity beyond. Note that the non-linear behavior is only a very gently bent, quasi linear curve.

Figure 11b compares the *normalized* predicted Young's modulus to the measured one, relative to the reference. That is, we divide each measured sample Young's modulus by the Young's modulus measured on the reference specimen. The overall behavior matches remarkably well, as the shapes of the curves closely correspond. The vertical offset between the measure and the prediction indicates that our samples are overall stiffer than expected. This is most likely explained by the fabrication process, and in particular by the imperfect infilling of the fabricated reference (changes to the reference stiffness moves the curve up/down).

We provide in the graph both numerical predictions (homogenized and detailed simulations). It is expected that the homogenized material is slightly different since it considers an infinite periodic medium. The close agreement between them shows that the samples are sufficiently large to capture the macroscale foam behavior.

We report the result of repeated compression tests in Figure 12. Compared to tensile tests, under compression the foams enter a non-linear regime after less deformation, which is due to the buckling of elongated edges. Nevertheless, all specimens exhibit a similar non-linear behavior that follows the same proportions as their Young's modulus ratios. Repeated testing of the same specimens reveal that after the first few tests the behavior changes in the non-linear regime – while it remains very similar in the linear one. Interestingly, subsequent tests behave more stably, indicating a burn-in behavior that converges towards a stable response. This could be explained by failures in places of high local stresses, which no longer influence the behavior after the first few compressions.

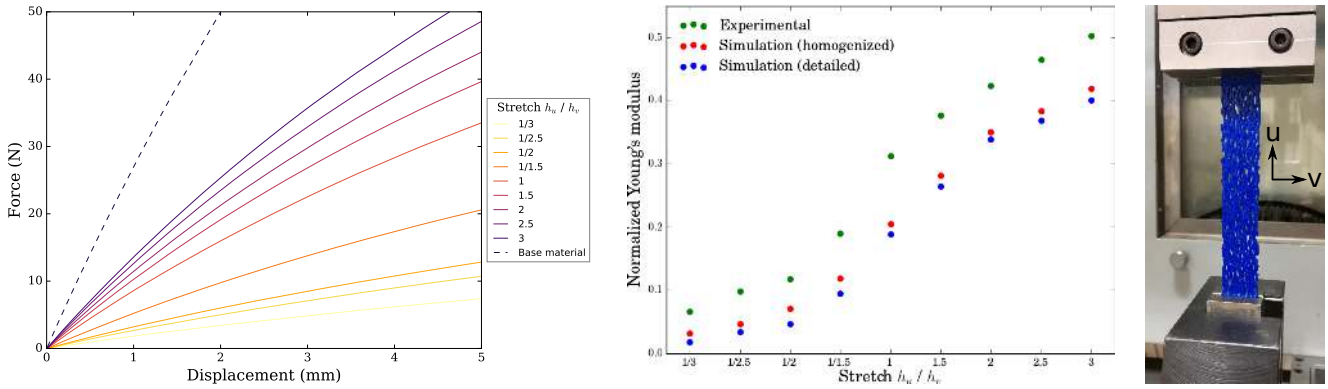

(a) (b) (c)

Fig. 11. Uniaxial tensile tests on a MTS® 4/ML testing machine, with a force sensor of 100 N, displacement speed of 1 mm/ min. The specimens have a dimension of 18×108 mm and thickness 3.2 mm. Nine of them correspond to varying ratios of stretch h_u/h_v, one is the reference base material. (a) Measured force/displacement curves (raw data). (b) Predicted (homogenized and detailed simulation) vs measured normalized Young's modulus. (c) Specimen with $h_u/h_v = 2$ being tested.

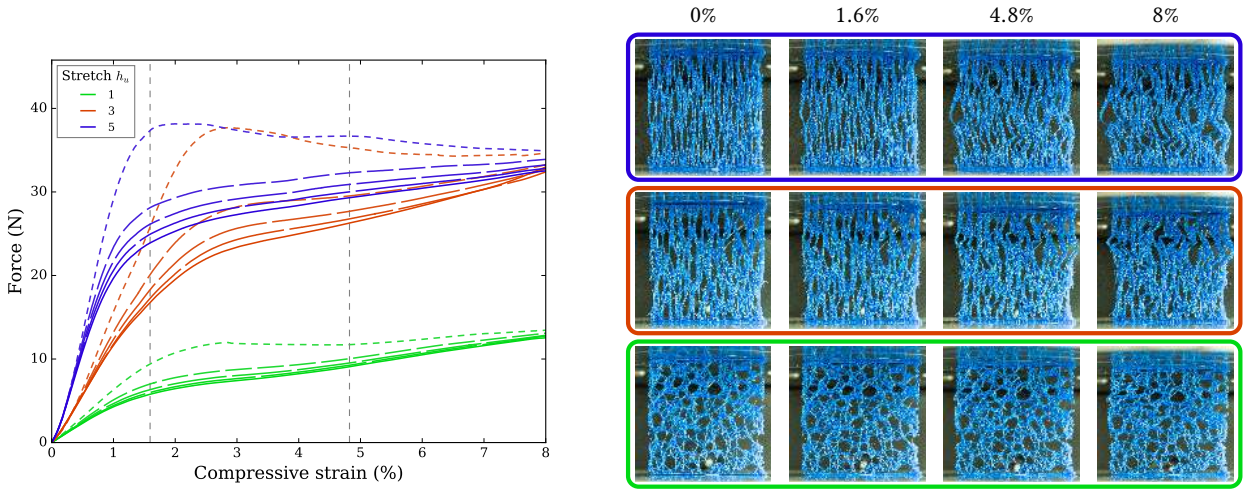

Fig. 12. Repeated compression tests with three prints having the same dimensions ($50 \times 50 \times 7$ mm) and using the same point density. The stretch varies in the vertical direction ($h_u = 1, 3, 5$). All the tests are performed on an Instron 3345 testing machine, with a force sensor of 500 N. The maximum compressive strain is 8% (4 mm), attained at a speed of 1 mm/ min. Each print is repeatedly tested five times, waiting for two minutes between each test. Please refer to the text for discussion. **Left:** The curves revealing the measured forces as the compressive strain increases. Short dashes correspond to first tests, while longer dashes indicate later tests. The vertical dashed lines corresponds to 1.6% and 4.8% strain. **Right:** From left to right, photos for increasing compressive strains.

We report in Figure 13 compression tests on 3D foam specimens.

6 APPLICATION TO ADDITIVE MANUFACTURING

In this section we discuss the use of our foams for the design of 3D objects with orthotropic elasticity. Figure 1 (left) illustrates an orthotropic chair design inspired from the work of designer Lilian van Daal. The initial foam design is two dimensional and generated within the chair profile. It is then extruded into the final object, producing orthotropy in the seat and the back.

Figure 1 (right) is an illustrative model of a gear made lighter by an orthotropic foam oriented against the surface, keeping it resistant to pressure. Figure 14 is a tree model with a foam oriented vertically, along the inner distance field, showing how longitudinal strength can be preserved. Figure 10 (right) illustrates a 3D printed cube of orthotropic foam, printed on a *B9 Creator* resin printer. The cube is $35 \times 35 \times 35$ millimeters with Young's moduli ratios of $E_z/E_y = 20.5, E_y/E_x = 8.4$, for stretch $h_x = 1.0, h_y = 2.0, h_z = 6.0$. Figure 15 show two cylinders filled with our foams and having different orthotropic behaviors. In each cylinder, the local stretch rigidifies one direction while making the other two more flexible.

Regarding results with deformations, please keep in mind our analysis is performed on linear elasticity (small deformations), and

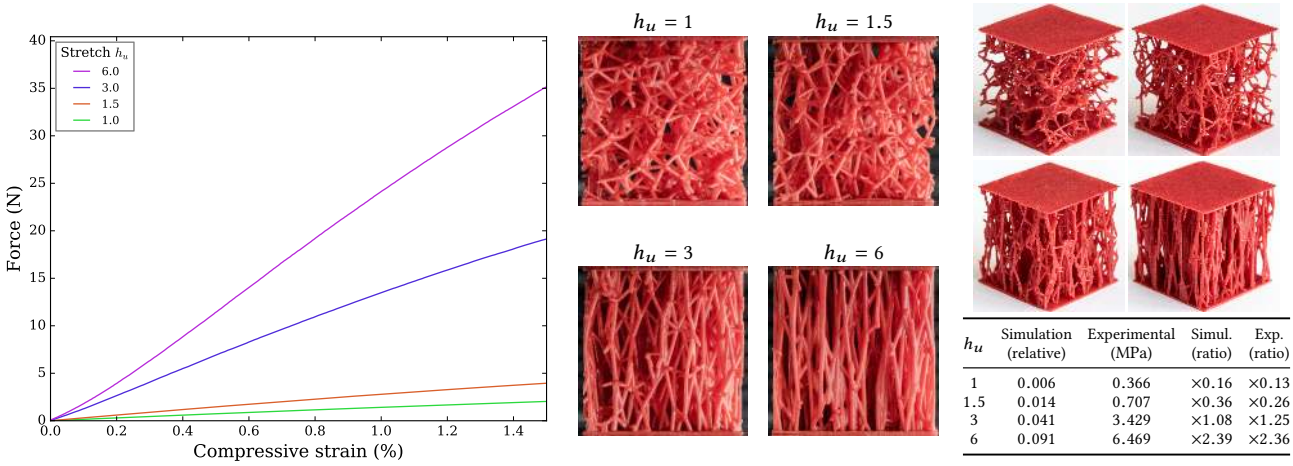

(a) (b)

h_u	Simulation (relative)	Experimental (MPa)	Simul. (ratio)	Exp. (ratio)
1	0.006	0.366	×0.16	×0.13
1.5	0.014	0.707	×0.36	×0.26
3	0.041	3.429	×1.08	×1.25
6	0.091	6.469	×2.39	×2.36

(c)

Fig. 13. Compression tests of 3D k-nearest foams with a beam radius of 0.25 mm within cubes of $20 \times 20 \times 20$ mm, printed on a B9Creator (DLP resin printer). To minimize errors due to the fabrication process all specimens were printed together and measured in one session. The stretch along the compression direction is different for each specimen ($h_u = 1, 1.5, 3, 6$), all other parameters are equal ($h_v = h_w = 1$). Tests are performed on an Instron 3345 testing machine. The compression speed is 0.5 mm/ min, the maximum compressive strain is 1.5 % using a high precision 50 N sensor. (a) Force measured as a function of relative compressive strain. (b) Pictures of the foams (front view, initial position). (c) The first two columns report the Young's modulus (E_z) for each specimen, for simulation (relative) and experiment (MPa). For comparison the two last columns show the ratios over the average value, for each column (i.e. how much more rigid/flexible each is with respect to the average). As can been seen the ratios agree well overall.

Fig. 14. 3D printed tree with internal orthotropic foam. The foam is oriented vertically along the surface.

Fig. 15. 3D printed cylinders with orthotropic material. **Top:** The center segment is made more rigid horizontally and flexible vertically. **Bottom:** The extremities are isotropic, the center is rigid along the main axis but flexible radially.

therefore we cannot predict large deformation behaviors accurately. Nevertheless, the designed structures trigger the expected global deformation. Under small deformations the analysis is accurate (see Figure 11 and 13).

Figure 16 illustrates how our foams can be used in conjunction with the results of topology optimization. We run the SIMP method [Bendsøe 1989] using a penalty of $p = 1$ (continuous material distribution) and a volume constraint of 40%. We then extract the stress field from the FEM simulation. Material density, principal stress direction and magnitude are mapped to the foam parameters.

While this case is essentially illustrative, we believe future integration of our foams within free material optimization methods will allow to further exploit the material space.

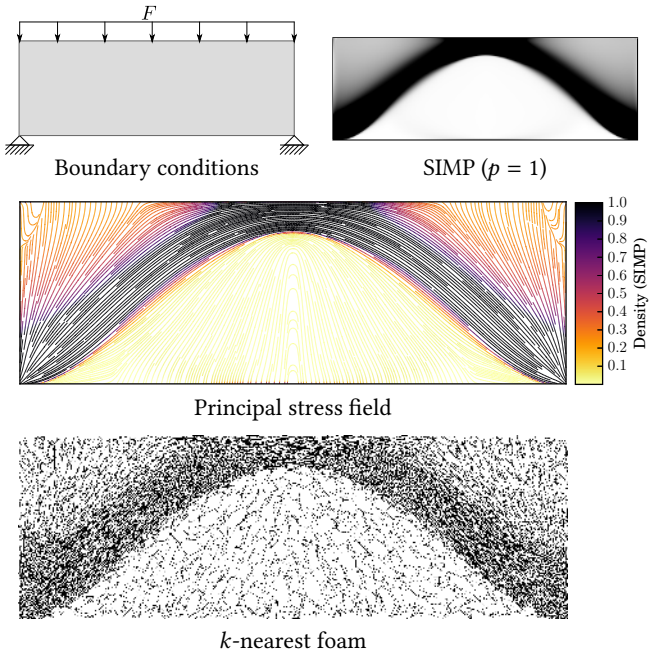

Fig. 16. Filling a design generated by topology optimization (SIMP [Bendsøe 1989]) with our foam. Orthotropy aligns with the main direction of stress. Density is controlled from the output of topology optimization.

7 LIMITATIONS AND FUTURE WORK

Our approach has a number of limitations and opportunities for future work. The range of Poisson's ratio spawned by the method, while quite large, remains positive. Whether or not stochastic structures with negative Poisson's ratios can be devised remains an open question. We do not provide any method to generate beams covering the modeled objects. This is more difficult than with cellular structures, where the cells have a geometric footprint that can be subtracted from the surface [Brennan-Craddock 2011]. Currently, we trim or cancel the beams crossing the surface, and optionally rely on a solid shell skin. Our foams print reliably on filament printers (extruded 2D foams) and powder based systems (SLS). While we did successfully print on SLA (resin) printers two over three prints, the foams do not fully comply with the requirements. In particular, the foam graphs might exhibit unsupported local minima with respect to the build direction. The number of local minima is very small : 0.57% of the graph nodes on average (does not depend on stretch, unless reaching extreme values, e.g. $h_u > 100$). We therefore trim these out prior to printing. The main difficulty are however the elongated near horizontal beams, which tend to move with resin tanks motion.

As future work, we would like to consider other properties such as large scale deformations, fatigue and crushing/rupture behaviors. Finally, we only consider single material prints. It would be interesting to investigate a similar methodology for the design of porous structures in a multi-material setting, with beams in different materials.

8 CONCLUSIONS

We presented a stochastic, procedural, orthotropic metamaterial which can produce elastic behaviors with a wide range of Young's moduli ratio along orthogonal directions. Thanks to its stochastic nature and aperiodicity, the material properties can be graded freely in space, both in terms of local frame orientation and Young's moduli along orthogonal directions. This is achieved by mapping physical properties back to the procedural generation parameters: angles, metric stretch, and density. The foam scales trivially through procedural generation.

While our foams can be used for a wide range of design tasks and to interpret the results of topology optimization, we believe a tighter integration can be achieved with free material optimization methods [Bendsøe et al. 1994; Kočvara and Stingl 2007], constraining the elasticity tensor to remain in the covered material space.

ACKNOWLEDGMENTS

We would like to thank Olivier Godard (Institut Jean Lamour, UMR 7198 CNRS – Université de Lorraine) for his help during mechanical experiments, Fabrice Neyret for valuable comments, and the anonymous reviewers for their useful suggestions. This work received support from Région Lorraine and FEDER.

REFERENCES

R. M. Jones. 1975. *Mechanics of Composite Materials.* Vol. 193. Scripta Book Company Washington, DC.

G. Allaire and G. A. Francfort. 1993. *A Numerical Algorithm for Topology and Shape Optimization.* Springer Netherlands, 239–248. DOI: https://doi.org/10.1007/978-94-011-1804-0_16

L. J. Gibson and M. F. Ashby. 1997. *Cellular Solids: Structure and Properties.* Cambridge university press.

G. Allaire. 2012. *Shape Optimization by the Homogenization Method.* Springer Science & Business Media.

E. Andreassen, B. S. Lazarov, and O. Sigmund. 2014. Design of Manufacturable 3D Extremal Elastic Microstructure. *Mechanics of Materials* 69, 1 (2014), 1–10. DOI: https://doi.org/10.1016/j.mechmat.2013.09.018

P. Balister, B. Bollobas, A. Sarkar, and M. Walters. 2005. Connectivity of Random k-nearest-neighbour Graphs. *Advances in Applied Probability* 37, 1 (2005), 1–24. DOI: https://doi.org/10.1017/s000186780000001x

M. P. Bendsøe. 1989. Optimal Shape Design as a Material Distribution Problem. *Struct. Optimization* 1, 4 (1989), 193–202. DOI: https://doi.org/10.1007/bf01650949

M. P. Bendsøe, J. Guedes, R. B. Haber, P. Pedersen, and J. Taylor. 1994. An Analytical Model to Predict Optimal Material Properties in the Context of Optimal Structural Design. *J. Appl. Mech.* 61, 4 (1994), 930–937. DOI: https://doi.org/10.1115/1.2901581

M. P. Bendsøe and N. Kikuchi. 1988. Generating Optimal Topologies in Structural Design Using a Homogenization Method. *Computer Methods in Applied Mechanics and Engineering* 71, 2 (1988), 197–224. DOI: https://doi.org/10.1016/0045-7825(88)90086-2

V. Bentkus and F. Götze. 1997. On the Lattice Point Problem for Ellipsoids. *Acta Arithmetica* 80, 2 (1997), 101–125. http://pldml.icm.edu.pl/pldml/element/bwmeta1.element.bwnjournal-article-aav80i2p101bwm

B. Bickel, M. Bächer, M. A. Otaduy, H. R. Lee, H. Pfister, M. Gross, and W. Matusik. 2010. Design and Fabrication of Materials With Desired Deformation Behavior. *ACM Trans. Graph.* 29, 4 (2010), 1. DOI: https://doi.org/10.1145/1778765.1778800

J. Brennan-Craddock. 2011. *The Investigation of a Method to Generate Conformal Lattice Structures for Additive Manufacturing.* Ph.D. Dissertation. Loughborough Univ. https://dspace.lboro.ac.uk/2134/9146

D. Chen, D. I. W. Levin, P. Didyk, P. Sitthi-Amorn, and W. Matusik. 2013. Spec2Fab: A Reducer-Tuner Model for Translating Specifications to 3D Prints. *ACM Trans. Graph.* 32, 4 (2013), 1. DOI: https://doi.org/10.1145/2461912.2461994

Y. Chen. 2007. 3D Texture Mapping for Rapid Manufacturing. *Comput. Aided Des. Appl.* 4, 6 (2007), 761–771. DOI: https://doi.org/10.1080/16864360.2007.10738509

Q. Du and D. Wang. 2005. Anisotropic Centroidal Voronoi Tessellations and Their Applications. *SIAM Journal on Scientific Computing* 26, 3 (2005), 737–761. DOI: https://doi.org/10.1137/S1064827503428527

H. A. Eschenauer and N. Olhoff. 2001. Topology Optimization of Continuum Structures: A Review. *Applied Mechanics Reviews* 54, 4 (2001), 331. DOI: https://doi.org/10.1115/

1.1388075
O. Fryazinov, T. Vilbrandt, and A. Pasko. 2013. Multi-Scale Space-Variant FRep Cellular Structures. *Computer-Aided Design* 45, 1 (2013), 26–34. DOI: https://doi.org/10.1016/j.cad.2011.09.007
G. H. Hardy. 1915. On the Expression of a Number as the Sum of Two Squares. *Quart. J. Math.* 46 (1915), 263–283.
A. Ion, J. Frohnhofen, L. Wall, R. Kovacs, M. Alistar, J. Lindsay, P. Lopes, H.-T. Chen, and P. Baudisch. 2016. Metamaterial Mechanisms. In *Proceedings of the 29th Annual Symposium on User Interface Software and Technology - UIST '16*. Association for Computing Machinery (ACM), 529–539. DOI: https://doi.org/10.1145/2984511.2984540
S. G. Johnson. 2016. The NLopt Nonlinear-Optimization Package. http://ab-initio.mit.edu/nlopt. (2016).
M. Kočvara and M. Stingl. 2007. Free Material Optimization for Stress Constraints. *Struct. Multidiscip. Opt.* 33, 4 (2007), 323–335. DOI: https://doi.org/10.1007/s00158-007-0095-5
B. Lévy and N. Bonneel. 2013. Variational Anisotropic Surface Meshing with Voronoi Parallel Linear Enumeration. In *Proc. of the 21st International Meshing Roundtable*. Springer Berlin Heidelberg. DOI: https://doi.org/10.1007/978-3-642-33573-0_21
D. Li, N. Dai, X. Jiang, and X. Chen. 2015. Interior Structural Optimization Based on the Density-Variable Shape Modeling of 3D Printed Objects. *The International Journal of Advanced Manufacturing Technology* 83, 9 (2015), 1627–1635. DOI: https://doi.org/10.1007/s00170-015-7704-z
Y. Li and J. Barbič. 2015. Stable Anisotropic Materials. *IEEE Trans. Vis. Comput. Graph.* 21, 10 (2015), 1129–1137. DOI: https://doi.org/10.1109/TVCG.2015.2448105
R. Lipton. 1994. Optimal Bounds on Effective Elastic Tensors for Orthotropic Composites. *Proceedings of the Royal Society of London A: Mathematical, Physical and Engineering Sciences* 444, 1921 (1994), 399–410. DOI: https://doi.org/10.1098/rspa.1994.0028
L. Lu, B. Chen, A. Sharf, H. Zhao, Y. Wei, Q. Fan, X. Chen, Y. Savoye, C. Tu, and D. Cohen-Or. 2014. Build-To-Last: Strength to Weight 3D Printed Objects. *ACM Trans. Graph.* 33, 4 (2014), 1–10. DOI: https://doi.org/10.1145/2601097.2601168
J. Martínez, J. Dumas, and S. Lefebvre. 2016. Procedural Voronoi Foams for Additive Manufacturing. *ACM Trans. Graph.* 35, 4 (2016), 44:1–44:12. DOI: https://doi.org/10.1145/2897824.2925922
M. Moakher and A. N. Norris. 2006. The Closest Elastic Tensor of Arbitrary Symmetry to an Elasticity Tensor of Lower Symmetry. *Journal of Elasticity* 85, 3 (2006), 215–263. DOI: https://doi.org/10.1007/s10659-006-9082-0
J. Panetta, Q. Zhou, L. Malomo, N. Pietroni, P. Cignoni, and D. Zorin. 2015. Elastic Textures for Additive Fabrication. *ACM Trans. Graph.* 34, 4 (2015), 135:1–135:12. DOI: https://doi.org/10.1145/2766937
O. Pantz and K. Trabelsi. 2008. A Post-Treatment of the Homogenization Method for Shape Optimization. *SIAM Journal on Control and Optimization* 47, 3 (2008), 1380–1398. DOI: https://doi.org/10.1137/070688900
A. Pasko, O. Fryazinov, T. Vilbrandt, P.-A. Fayolle, and V. Adzhiev. 2011. Procedural Function-Based Modelling of Volumetric Microstructures. *Graphical Models* 73, 5 (2011), 165–181. DOI: https://doi.org/10.1016/j.gmod.2011.03.001
P. Pedersen. 1989. On Optimal Orientation of Orthotropic Materials. *Struct. Optimization* 1, 2 (1989), 101–106. DOI: https://doi.org/10.1007/BF01637666
A. Radman, X. Huang, and Y. M. Xie. 2013. Topology Optimization of Functionally Graded Cellular Materials. *Journal of Materials Science* 48, 4 (2013), 1503–1510. DOI: https://doi.org/10.1007/s10853-012-6905-1
J. Robbins, S. Owen, B. Clark, and T. Voth. 2016. An Efficient and Scalable Approach for Generating Topologically Optimized Cellular Structures for Additive Manufacturing. *Additive Manufacturing* 12, B (2016), 296–304. DOI: https://doi.org/10.1016/j.addma.2016.06.013
A. P. Roberts and E. J. Garboczi. 2002. Elastic Properties of Model Random Three-Dimensional Open-Cell Solids. *J. Mech. Phys. Solids* 50, 1 (2002), 33–55. DOI: https://doi.org/10.1016/s0022-5096(01)00056-4
D. W. Rosen. 2007. Computer-Aided Design for Additive Manufacturing of Cellular Structures. *Computer-Aided Design and Applications* 4, 5 (2007), 585–594. DOI: https://doi.org/10.1080/16864360.2007.10738493
G. I. N. Rozvany. 2001. Aims, Scope, Methods, History and Unified Terminology of Computer-Aided Topology Optimization in Structural Mechanics. *Struct. Multidiscip. Opt.* 21, 2 (2001), 90–108. DOI: https://doi.org/10.1007/s001580050174
C. Schumacher, B. Bickel, J. Rys, S. Marschner, C. Daraio, and M. Gross. 2015. Microstructures to Control Elasticity in 3D Printing. *ACM Trans. Graph.* 34, 4 (2015), 136:1–136:13. DOI: https://doi.org/10.1145/2766926
O. Sigmund. 1994. Materials With Prescribed Constitutive Parameters: An Inverse Homogenization Problem. *Int. J. Solids Struct.* 31, 17 (1994), 2313–2329. DOI: https://doi.org/10.1016/0020-7683(94)90154-6
O. Sigmund. 1995. Tailoring Materials With Prescribed Elastic Properties. *Mechanics of Materials* 20, 4 (1995), 351–368. DOI: https://doi.org/10.1016/0167-6636(94)00069-7
O. Sigmund and S. Torquato. 1999. Design of Smart Composite Materials Using Topology Optimization. *Smart Materials and Structures* 8, 3 (1999), 365. http://stacks.iop.org/0964-1726/8/i=3/a=308
M. Skouras, B. Thomaszewski, S. Coros, B. Bickel, and M. Gross. 2013. Computational Design of Actuated Deformable Characters. *ACM Trans. Graph.* 32, 4 (2013), 1. DOI: https://doi.org/10.1145/2461912.2461979
K. Suzuki and N. Kikuchi. 1991. A Homogenization Method for Shape and Topology Optimization. *Comput. Method. Appl. M.* 93, 3 (1991), 291–318. DOI: https://doi.org/10.1016/0045-7825(91)90245-2
T. Ting. 1996. Positive Definiteness of Anisotropic Elastic Constants. *Math. Mech. Solids* 1, 3 (1996), 301–314. DOI: https://doi.org/10.1177/108128659600100302
T. C. T. Ting and T. Chen. 2005. Poisson's Ratio for Anisotropic Elastic Materials Can Have No Bounds. *Q. J. Mech. Appl. Math.* 58, 1 (2005), 73–82. DOI: https://doi.org/10.1093/qjmamj/hbh021
K. Vidimče, A. Kaspar, Y. Wang, and W. Matusik. 2016. Foundry: Hierarchical Material Design for Multi-Material Fabrication. In *Proc. of the 29th Annual Symposium on User Interface Software and Technology–UIST'16*. ACM, New York, NY, USA, 563–574. DOI: https://doi.org/10.1145/2984511.2984516
K. Vidimče, S.-P. Wang, J. Ragan-Kelley, and W. Matusik. 2013. OpenFab: A Programmable Pipeline for Multi-Material Fabrication. *ACM Trans. Graph.* 32, 4 (2013), 1. DOI: https://doi.org/10.1145/2461912.2461993
H. Wang, Y. Chen, and D. W. Rosen. 2005. A Hybrid Geometric Modeling Method for Large Scale Conformal Cellular Structures. In *Volume 3: 25th Computers and Information in Engineering Conference, Parts A and B*. 421–427. DOI: https://doi.org/10.1115/DETC2005-85366
W. Wang, T. Y. Wang, Z. Yang, L. Liu, X. Tong, W. Tong, J. Deng, F. Chen, and X. Liu. 2013. Cost-Effective Printing of 3D Objects With Skin-Frame Structures. *ACM Trans. Graph.* 32, 6 (2013), 1–10. DOI: https://doi.org/10.1145/2508363.2508382
S. Worley. 1996. A Cellular Texture Basis Function. In *Proceedings of the 23rd annual conference on Computer graphics and interactive techniques - SIGGRAPH '96*. ACM, New York, NY, USA, 291–294. DOI: https://doi.org/10.1145/237170.237267
J. Wu, N. Aage, R. Westermann, and O. Sigmund. 2016a. Infill Optimization for Additive Manufacturing–Approaching Bone-Like Porous Structures. *arXiv* (2016). http://arxiv.org/abs/1608.04366
J. Wu, C. C. Wang, X. Zhang, and R. Westermann. 2016b. Self-Supporting Rhombic Infill Structures for Additive Manufacturing. *Computer-Aided Design* 80 (2016), 32–42. DOI: https://doi.org/10.1016/j.cad.2016.07.006
L. Xia and P. Breitkopf. 2015. Design of Materials Using Topology Optimization and Energy-Based Homogenization Approach in Matlab. *Struct. Multidiscip. Opt.* 52, 6 (2015), 1229–1241. DOI: https://doi.org/10.1007/s00158-015-1294-0
H. Xu, Y. Li, Y. Chen, and J. Barbič. 2015. Interactive Material Design Using Model Reduction. *ACM Trans. Graph. (TOG)* 34, 2 (2015), 18. DOI: https://doi.org/10.1145/2699648
F. Xue and P. Kumar. 2004. The Number of Neighbors Needed for Connectivity of Wireless Networks. *Wireless Networks* 10, 2 (2004), 169–181. DOI: https://doi.org/10.1023/B:WINE.0000013081.09837.c0
X. Zhang, Y. Xia, J. Wang, Z. Yang, C. Tu, and W. Wang. 2015. Medial Axis Tree—an Internal Supporting Structure for 3D Printing. *Computer Aided Geometric Design* 35-36 (2015), 149–162. DOI: https://doi.org/10.1016/j.cagd.2015.03.012
S. Zhou and Q. Li. 2008. Design of Graded Two-Phase Microstructures for Tailored Elasticity Gradients. *Journal of Materials Science* 43, 15 (2008), 5157–5167. DOI: https://doi.org/10.1007/s10853-008-2722-y